Commun. Comput. Phys.
doi: 10.4208/cicp.2014.m385

Vol. **17**, No. 5, pp. 1271-1300
May 2015

Three-Dimensional Simulation of Balloon Dynamics by the Immersed Boundary Method Coupled to the Multiple-Relaxation-Time Lattice Boltzmann Method

Jiayang Wu, Yongguang Cheng*, Chunze Zhang and Wei Diao

State Key Laboratory of Water Resources and Hydropower Engineering Science, Wuhan University, Wuhan 430072, P.R. China.

Received 24 November 2013; Accepted (in revised version) 9 October 2014

Abstract. The immersed boundary method (IBM) has been popular in simulating fluid structure interaction (FSI) problems involving flexible structures, and the recent introduction of the lattice Boltzmann method (LBM) into the IBM makes the method more versatile. In order to test the coupling characteristics of the IBM with the multiple-relaxation-time LBM (MRT-LBM), the three-dimensional (3D) balloon dynamics, including inflation, release and breach processes, are simulated. In this paper, some key issues in the coupling scheme, including the discretization of 3D boundary surfaces, the calculation of boundary force density, and the introduction of external force into the LBM, are described. The good volume conservation and pressure retention properties are verified by two 3D cases. Finally, the three FSI processes of a 3D balloon dynamics are simulated. The large boundary deformation and oscillation, obvious elastic wave propagation, sudden stress release at free edge, and recoil phenomena are all observed. It is evident that the coupling scheme of the IBM and MRT-LBM can handle complicated 3D FSI problems involving large deformation and large pressure gradients with very good accuracy and stability.

AMS subject classifications: 76M28, 74F10

Key words: Immersed boundary method, multiple-relaxation-time lattice Boltzmann method, fluid-structure interaction, verification, balloon dynamics.

1 Introduction

Interactions between fluids and elastic objects are ubiquitous in nature, but efficient numerical techniques for investigating this kind of phenomena are challenging, however the immersed boundary method (IBM) has shown to be a powerful alternative model for simulating the problems. The IBM was originally developed by Peskin in 1972 to

*Corresponding author. *Email address:* ygcheng@whu.edu.cn (Y. G. Cheng), 760816021@qq.com (J. Y. Wu), zhangchunze@whu.edu.cn (C. Z. Zhang), wdiao@whu.edu.cn (W. Diao)

 ©2015 Global-Science Press

https://doi.org/10.4208/cicp.2014.m385 Published online by Cambridge University Press

simulate flow patterns around natural heart valves [1]. Unlike the traditional numerical methods for fluid structure interaction (FSI) that have to treat body-fitted and moving grid with great effort at every time step, the IBM is very simple and convenient, because it uses regular and uniform algorithms for moving boundaries. In the IBM, an Eulerian description of the Navier-Stokes (N-S) equations is used for the fluid dynamics and an Lagrangian description of elastic structural mechanics is used for the objects immersed in the fluid; the grid for discretizing the immersed boundary need not to be coincident with the underlying fluid mesh; the interaction between fluid and boundary is implemented by a discrete Dirac delta function, which spreads the force of the distorted elastic boundary to the nearby fluid nodes and interpolates from the local fluid velocity to update the boundary position; no special effort is needed in treating boundary movements in the simulation. Since Peskin's pioneering work, great progress in algorithm improvements and applications has been made. Applications such as blood flow in the human heart [2], FSI of natural and prosthetic cardiac valves [3], swimming of bacterial organisms and aquatic animals [4,5], platelet aggregation [6,7], deformation of three dimensional capsules [8,9], filament flapping dynamics [10,11,30] and parachute opening dynamics [13,14], have exhibited its effectiveness and great potential for simulating realistic and sophisticated FSI problems involving complicated, fast moving, and strongly deforming boundaries. However the existing versions of the IBM leave something to be desired: boundary accuracy and numerical stability may be further improved.

Because the fluid flow equations in the IB methods must be solved in a regular Cartesian grid, it is natural to think of replacing the original fast Fourier transform or project method based solvers IBM by the newly developed lattice Boltzmann method (LBM) [15,16]. The LBM is a regular lattice-based scheme for fluid flow simulations, and its easy implementation, intrinsic parallelism, and high accuracy for numerous fluid flow problems have been demonstrated by many works [17–19]. In the light of these advantages, introducing the LBM into the IBM to simulate FSI problems seems to be very attractive. The fact that both the IBM and LBM work on a regular lattice makes the IBM+LBM coupling possible and easy. The first work on IBM+LBM coupling was by Feng and Michaelides [20], who successfully simulated the sedimentation of many particles under gravity, and demonstrated the effectiveness of their IBM+LBM coupling scheme. Afterwards, some applications and improvements of the method were conducted. Zhang [7] simulated red blood cell aggregation. Cheng [21] analyzed the mitral valve flow. Tian [22] modeled the multiple elastic filament flapping. Dupuis [23] studied the flow past an impulsively started cylinder. Niu [24] improved the calculation of the boundary force on the fluid. Peng [25] carried out comparative study of the IBM+LBM and LBM bounce-back treatment of boundary. Kang [26] compared direct-forcing IBM+LBM methods for stationary complex boundaries. Cheng [27] improved the volume conservation and computational efficiency of the IBM+LBM coupling scheme by introducing a second-order treatment of the unsteady and non-uniform forcing terms into the LBM. Wu [28] made a velocity correction by using the external forcing term proposed by Guo [29] to guarantee the non-slip boundary condition. It should be noted that the works mentioned

https://doi.org/10.4208/cicp.2014.m385 Published online by Cambridge University Press

above are all for two-dimensional problems. In three dimensions, Krüger [9] simulated the deformation of an initially spherical capsule freely suspended in simple shear flow and studied some influence factors. Hao and Zhu [12] proposed both explicit and implicit schemes to simulate 3D viscous flow past deformable sheets and flags. Despite of good ability in simulating FSI phenomena, the IBM+LBM coupling scheme still suffers from numerical instability, volume leakage, and boundary slip, which are partly related to the LBM models.

Within the LBM models, the single-relaxation-time (SRT) version (SRT-LBM) is popular because of its simplicity, but its numerical stability and accuracy are not satisfactory [31, 32]. The multiple-relaxation-time (MRT) version (MRT-LBM) is relatively new and has better characteristics [32], especially the enhanced stability. Therefore, substituting the MRT-LBM for the SRT-LBM in the aforementioned IBM+LBM coupling schemes is promising, because the IBM+MRT-LBM scheme may overcome some drawbacks of the IBM+SRT-LBM scheme. Peng [33] first used an IBM+MRT-LBM to enhance the stability based on local grid refinement. Niu [24] introduced momentum exchange method into IBM+MRT-LBM to calculate Lagrangian force of rigid objects. Peng [34] proposed a 3D IBM+MRT-LBM for transportation of deformable particles in fluids and studied the flow-induced deformation and shape recovery of biconcave capsules. These first attempts are valuable and insightful. However, more three-dimensional IBM+MRT-LBM applications concerning problems of strongly deforming and fast moving boundaries need to be conducted.

In this paper, we propose an IBM+MRT-LBM method and apply it to three dimensional simulation of the balloon dynamics, which include three strong FSI processes: inflation, breach, and release. The fundamental physical phenomena, such as elastic wave propagation, recoil effect, and boundary oscillation mode, will be demonstrated. Some key treatments or techniques to guarantee simulation accuracy and stability will be discussed.

The rest of the paper is organized as follows. Section 2 briefly describes the basic formulation of the IBM+MRT-LBM scheme, including the governing equations and their discretization, followed by a short discussion about the boundary force calculation in the IBM and the external forcing term treatment in the LBM. Section 3 verifies the accuracy of the proposed IBM+MRT-LBM scheme by some typical benchmark problems. Section 4 presents the simulated dynamic processes of a three-dimensional balloon. And Section 5 concludes the paper.

2 The coupling scheme of IBM and MRT-LBM

2.1 The IBM for flexible boundary

2.1.1 The idea and formulation of IBM

In the IBM, an Eulerian description of the N-S equations is used for fluid dynamics, and a Lagrangian description of curvilinear boundaries is used for structural mechanics of

https://doi.org/10.4208/cicp.2014.m385 Published online by Cambridge University Press

objects immersed in the fluid. The formulation may be expressed as follows [35]:

$$\frac{\partial \rho}{\partial t}+\nabla\cdot(\rho\mathbf{u})=0, \tag{2.1}$$

$$\frac{\partial(\rho\mathbf{u})}{\partial t}+\nabla\cdot(\rho\mathbf{u}\mathbf{u})=-\nabla p+v\nabla\cdot[\rho(\nabla\mathbf{u}+(\nabla\mathbf{u})^T)]+\mathbf{f}, \tag{2.2}$$

$$\frac{d\mathbf{X}(q,r,s,t)}{dt}=\mathbf{U}(\mathbf{X},t)=\int_{\Omega_f}\mathbf{u}(\mathbf{x},t)\delta(\mathbf{x}-\mathbf{X}(q,r,s,t))d\mathbf{x}, \tag{2.3}$$

$$\mathbf{F}(q,r,s,t)=S_f\mathbf{X}(q,r,s,t), \tag{2.4}$$

$$\mathbf{f}(\mathbf{x},t)=\int_{\Gamma_b}\mathbf{F}(q,r,s,t)\delta(\mathbf{x}-\mathbf{X}(q,r,s,t))dqdrds, \tag{2.5}$$

where $\mathbf{X}$, $\mathbf{F}$ and $\mathbf{U}$ are the Lagrangian boundary position, boundary force density, and boundary moving speed, respectively; $\mathbf{x}$, $\mathbf{f}$, $\mathbf{u}$, p, ρ and v are the Eulerian spatial coordinate, external force density, flow velocity, flow pressure, fluid density, and kinematic viscosity, respectively; (q,r,s) is the Lagrangian curvilinear coordinates of the boundary, $\delta(r)$ is the Dirac delta function, and S_f is the boundary force generation operator. Eqs. (2.1) and (2.2) are the N-S equations with external force $\mathbf{f}$ in Eulerian form for the fluid flow in domain Ω_f, while Eqs. (2.3), (2.4) and (2.5) are the immersed boundary dynamic equations in Lagrangian form for the boundary Γ_b. The left side of Eq. (2.3) is the kinematic description of the immersed boundary, while Eq. (2.4) represents the constitutive law of the elastic boundary. The interaction of the fluid and the immersed boundary is realized by the Dirac delta function $\delta(r)$ in Eqs. (2.3) and (2.5), in which the former is used to impose the flow velocity $\mathbf{u}$ on the boundary and the latter is used to spread the boundary force $\mathbf{F}$ to the nearby fluid nodes.

The above equations are solved on a pair of computational grids: a cell centered uniform Cartesian grid for the Eulerian fluid flow variables and an unstructured triangular grid for the Lagrangian boundary variables. Let n be the time step index, and define the coordinates of the i, j, k-th Eulerian grid node as

$$\mathbf{x}_{ijk}=((i+1/2)\Delta x,(j+1/2)\Delta y,(k+1/2)\Delta z),$$

where Δx, Δy and Δz are the lattice spacings in x, y and z directions, respectively. Thus $\mathbf{u}^n_{ijk}$ denotes the value of $\mathbf{u}$ at $\mathbf{x}_{ijk}$ and time n. The Lagrangian grid-points are identified by a single index m. Thus $\mathbf{F}^n_m$ denotes the value of $\mathbf{F}$ at the m-th grid point $\mathbf{X}^n_m$ and time n.

The interaction between fluid nodes and boundary grid-points, governed by the integration against the Dirac delta function in Eqs. (2.3) and (2.5), is handled by introducing a regularized discrete delta function δ_h. The discretized forms of Eqs. (2.3) and (2.5), by using δ_h, may be expressed as

$$\frac{\mathbf{X}^{n+1}_m-\mathbf{X}^n_m}{\Delta t}=\sum_{i,j,k}\mathbf{u}^{n+1}_{ijk}\delta_h(\mathbf{x}_{ijk}-\mathbf{X}^n_m)h^3, \tag{2.6}$$

$$\mathbf{f}^n_{ijk}=\sum_m\mathbf{F}^n_m\delta_h(\mathbf{x}_{ijk}-\mathbf{X}^n_m)\Delta q\Delta r\Delta s, \tag{2.7}$$

https://doi.org/10.4208/cicp.2014.m385 Published online by Cambridge University Press

where $h=\Delta x=\Delta y=\Delta z$, and $\Delta q\Delta r\Delta s$ represents the boundary surface area defined on each Lagrangian point. Because the unstructured triangular mesh for the immersed boundary is used in our simulation, the above surface area is defined as one third of the total surface area of the neighboring triangles that have $\mathbf{X}_m^n$ as the common vertex. Theoretically, to prevent fluid leakage across the boundary, $|\mathbf{X}(q+\Delta q,r,s,t)-\mathbf{X}(q,r,s,t)|<h/2$ should be imposed, with similar restrictions for Δr and Δs.

The discrete delta function δ_h, appearing in Eqs. (2.6) and (2.7), is a smoothed approximation to the Dirac delta function $\delta(r)$. The detailed derivation and several specific forms can be found in literature [35]. We apply the commonly used form as follows:

$$\delta_h(x,y,z)=\frac{1}{h^3}\phi\left(\frac{x}{h}\right)\phi\left(\frac{y}{h}\right)\phi\left(\frac{z}{h}\right), \tag{2.8}$$

$$\phi(r)=\begin{cases}(3-2|r|+\sqrt{1+4|r|-4r^2})\Big/8, & 0\le|r|<1,\\ (5-2|r|-\sqrt{-7+12|r|-4r^2})\Big/8, & 1\le|r|<2,\\ 0, & |r|\ge 2.\end{cases} \tag{2.9}$$

2.1.2 Boundary model and force computation

In order to solve N-S equations with external force, we need to know the Lagrangian force defined on each Lagrangian point, which should properly reflect the geometrical variation of the boundary to the reference configuration. Currently, there are many ways to calculate the boundary force in three dimensions. Zhu [11] used structured rectangular mesh to discretize their elastic plate so that the stretching and bending energy, as well as the corresponding forces, can be discretized along the longitudinal and lateral directions. We found that this method may not serve as a suitable discretization strategy when it is applied to three-dimensional complicated boundaries such as spheroid or ellipsoid, because of the irregularity and nonuniformity of the grid. On the other hand, the methods introduced in literature [9,36–39] are based on the elastic mechanics and can handle immersed boundaries with arbitrary configurations. Here we adopt the method developed in reference [9] because it is very simple and can be easily incorporated into the framework of the IBM-LBM coupling scheme. The details are described below.

Since the immersed boundary we consider in all of our simulations has zero bending stiffness, the total energy of the membrane W only consists of the strain energy which can be expressed as $W=\int w^s dA$, where w^s is the strain energy density, and dA is the surface element. For the elastic membrane that follows the neo-Hookean law, the constitutive law is given by

$$w^s=\frac{E}{6}\left(I_1+\frac{1}{I_2+1}-1\right), \tag{2.10}$$

in which E is the elastic modulus, and I_1 and I_2 are the first and second strain invariants,

https://doi.org/10.4208/cicp.2014.m385 Published online by Cambridge University Press

respectively. I_1 and I_2 depend on the local principal in-plane stretch ratio λ_1 and λ_2

$$I_1=\lambda_1^2+\lambda_2^2-2, \tag{2.11}$$

$$I_2=\lambda_1^2\lambda_2^2-1. \tag{2.12}$$

More information about this constitutive law can be found in literature [8, 40]. In all of our simulations, elastic boundaries are governed by Eq. (2.10).

The calculation of the strain energy density requires the knowledge of strain invariants, which can be calculated by the following procedures. As shown in Fig. 1, we first use a set of flat triangular elements to discretize the immersed boundary, and assume that the elements remain flat even under large membrane deformation. Second, we transform the deformed triangular element and its corresponding undeformed one to a common plane using rotations and translations as shown in Fig. 2. It should be pointed out that this transformation will not change the strain energy stored in the element. Once the deformed and undeformed element are transformed to the common plane, the next assumption we need is that the displacement gradient tensor is spatially constant over the entire triangular element, which can be achieved by introducing the shape function $N_i(x,y)=a_ix+b_iy+c_i$ $(i=1,2,3)$ defined on each node. The coefficients in the shape function can be determined by using the important property $N_i(x_j,y_j)=\delta_{ij}$ $(i,j=1,2,3)$. With the help of the shape function we can transfer any variables defined on the node to the element, for example, displacements can be calculated by $v(x,y)=N_1v_1+N_2v_2+N_3v_3$, and displacement gradient tensor can then be found by differentiating. It is straightforward to show that the displacement gradient tensor has the form [9]

$$(D_{\alpha\beta})=\begin{pmatrix} a & b \\ 0 & c \end{pmatrix}, \quad a=\frac{l}{l_0}, \quad b=\frac{1}{\sin\varphi_0}\left(\frac{l'}{l_0'}\cos\varphi-\frac{l}{l_0}\cos\varphi_0\right), \quad c=\frac{l'}{l_0'}\frac{\sin\varphi}{\sin\varphi_0}. \tag{2.13}$$

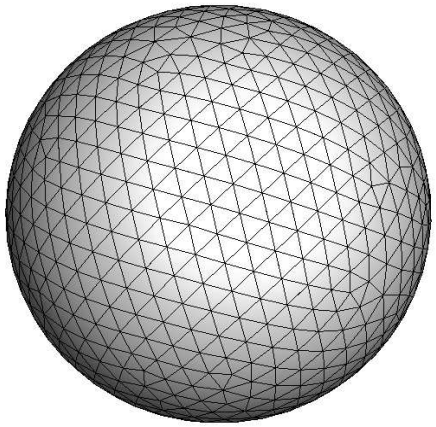


Figure 1: Discretization of a sphere by triangular elements.

https://doi.org/10.4208/cicp.2014.m385 Published online by Cambridge University Press

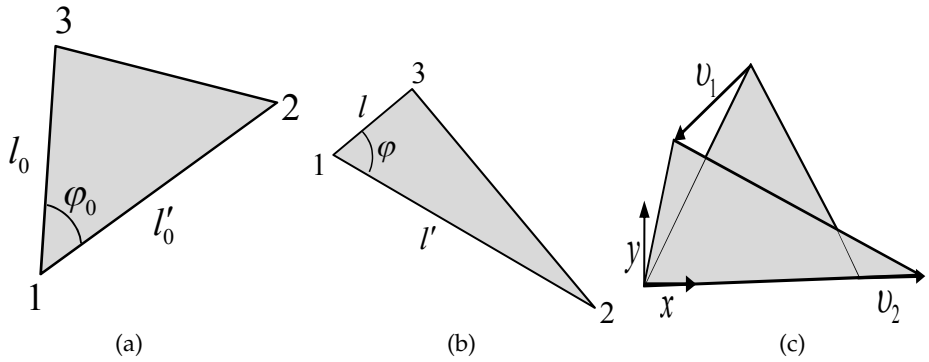


Figure 2: Illustration of the strain calculation of an element. (a) The equilibrium face, (b) The deformed shape, and (c) The deformation metric.

The coefficients in Eq. (2.13) are shown in Fig. 2. Once we get the displacement gradient tensor, the stain invariants can be calculated using the following relations [36, 37]:

$$\lambda_1^2+\lambda_2^2=\mathrm{tr}\mathbf{D}^T\mathbf{D}=a^2+b^2+c^2, \tag{2.14}$$

$$\lambda_1^2\lambda_2^2=\det\mathbf{D}^T\mathbf{D}=a^2c^2. \tag{2.15}$$

Then Eq. (2.10) is used to determine the strain energy density. The total energy of the elastic membrane can then be computed according to

$$W=\sum_i^{faces} A_{0i}w_i^s, \tag{2.16}$$

where A_{0i} is the area of the triangular element i under stress-free state. Once the total energy is known, the Lagrangian force defined on node m with its Eulerian coordinate $\mathbf{X}_m$ can be calculated from the principle of virtual work,

$$\mathbf{F}_m=-\frac{\partial W(\mathbf{X}_m)}{\partial \mathbf{X}_m}. \tag{2.17}$$

In order to model the interaction of fluid and rigid body, such as the fixed blowing pipe in our balloon inflation case (see below), we adopt a penalty approach by which the boundary force density $\mathbf{F}_m$ can be computed as

$$\mathbf{F}_m=-k_f(\mathbf{X}_m-\mathbf{Z}_m), \tag{2.18}$$

where k_f is the fastening stiffness and $\mathbf{Z}_m$ is the fastening or target position of point m. This equation may also be used to define the tethering effect, because it describes a spring connecting the Lagrangian point and its target position, with k_f being a spring constant and $\mathbf{X}_m-\mathbf{Z}_m$ being the spring length.

https://doi.org/10.4208/cicp.2014.m385 Published online by Cambridge University Press

2.2 The LBM for fluid flow

2.2.1 Basic formulation of LBM with multi-relaxation-time collision

The most common LBM model for three-dimensional simulations is the one using a square lattice with nineteen discrete velocity directions (denoted as model D3Q19). The discretized form of the lattice Boltzmann equation with multi-relaxation-time collision operator can be written as [31]

$$f_\alpha(\mathbf{x}+\mathbf{e}_\alpha\delta_t,t+\delta_t)-f_\alpha(\mathbf{x},t)=-M^{-1}\widehat{S}[m_\alpha(\mathbf{x},t)-m_\alpha^{eq}(\mathbf{x},t)]+\delta_t F_\alpha \quad \alpha=0,1,\cdots,18, \tag{2.19}$$

where $\{f_\alpha(\mathbf{x},t):\alpha=0,1,\cdots,18\}$ are the discrete distribution functions at position $\mathbf{x}$ and time t; $\{F_\alpha:\alpha=0,1,\cdots,18\}$ are the external forcing term which need special treatment in the IBM+LBM scheme and will be discussed in the next section; $\{m_\alpha(\mathbf{x},t):\alpha=0,1,\cdots,18\}$ are the moments of the distribution functions and may be expressed as

$$m=(\rho,e,\varepsilon,j_x,q_x,j_y,q_y,j_z,q_z,3p_{xx},3\pi_{xx},p_{ww},\pi_{ww},p_{xy},p_{yz},p_{xz},m_x,m_y,m_z)^T.$$

The physical meanings of the above moments can be found in literature [31]. The relation between m and distribution function f may be expressed as

$$m=Mf, \tag{2.20}$$

where M is the transformation matrix which can be constructed by the Gram-Schmidt orthogonalization procedure from discrete velocity set [31]. The diagonal collision matrix may be given as

$$\widehat{S}=diag(0,s_1,s_2,0,s_4,0,s_4,0,s_4,s_9,s_{10},s_9,s_{10},s_{13},s_{13},s_{13},s_{16},s_{16},s_{16}). \tag{2.21}$$

In the SRT collision approximation, the above parameters are set to be a single value, while in the MRT-LBM they are determined by linear stability analysis in order to significantly improve numerical stability and accuracy [32]. The equilibria of the moments m^{eq} as of $\rho^{eq}=\rho$ and $\mathbf{j}^{eq}=\mathbf{j}$ are given by

$$e^{eq}=-11\rho+\frac{19}{\rho_0}\mathbf{j}\cdot\mathbf{j}, \tag{2.22}$$

$$\varepsilon^{eq}=3\rho-\frac{11}{2\rho_0}\mathbf{j}\cdot\mathbf{j}, \tag{2.23}$$

$$q_x^{eq}=-\frac{2}{3}j_x,\quad q_y^{eq}=-\frac{2}{3}j_y,\quad q_z^{eq}=-\frac{2}{3}j_z, \tag{2.24}$$

$$p_{xx}^{eq}=\frac{1}{3\rho_0}[2j_x^2-(j_y^2+j_z^2)],\quad p_{ww}^{eq}=\frac{1}{\rho_0}[j_y^2-j_z^2], \tag{2.25}$$

$$p_{xy}^{eq}=\frac{1}{\rho_0}j_xj_y,\quad p_{yz}^{eq}=\frac{1}{\rho_0}j_yj_z,\quad p_{zx}^{eq}=\frac{1}{\rho_0}j_zj_x, \tag{2.26}$$

$$\pi_{xx}^{eq}=-\frac{1}{2}p_{xx}^{eq},\quad \pi_{ww}^{eq}=-\frac{1}{2}p_{ww}^{eq}, \tag{2.27}$$

$$m_x^{eq}=m_y^{eq}=m_z^{eq}=0, \tag{2.28}$$

https://doi.org/10.4208/cicp.2014.m385 Published online by Cambridge University Press

where ρ_0 is the mean density and usually set to be unity in simulations. The replacement of ρ_0 for ρ in the above equation suggests that the model we use here is incompressible. The bulk and kinematic viscosity of the model are

$$\zeta = \frac{2}{9}\left(\frac{1}{s_1} - \frac{1}{2}\right), \tag{2.29}$$

$$v = \frac{1}{3}\left(\frac{1}{s_9} - \frac{1}{2}\right). \tag{2.30}$$

In this paper, the relaxation parameters are given as $s_1 = 1.19$, $s_2 = s_{10} = 1.4$, $s_4 = 1.2$, $s_{16} = 1.98$, while $s_9 = s_{13}$ are determined according to kinematic viscosity. The density ρ and the velocity $\mathbf{u}$ are defined as

$$\rho = \sum_\alpha f_\alpha, \quad \rho_0 \mathbf{u} = \sum_\alpha \mathbf{e}_\alpha f_\alpha. \tag{2.31}$$

2.2.2 The introduction of external force into LBM

The approach of handling the external forcing term in the lattice Boltzmann equation (2.19) has great influence on the performance of the IBM in terms of volume conservation, numerical accuracy near the immersed boundary, and stability. Using a regular treatment of external forcing term may lead to instability even at the early stage of simulation [27]. In this paper, we follow Cheng [41] in treating the external forcing term, which not only can introduce unsteady and non-uniform body forces into the momentum equations, but also is able to add an arbitrary source term into the continuity equation. Assuming that A is the source term in the continuity equation and $\mathbf{B}$ is the external forcing term in the momentum equations, the scheme proposed by Cheng may be written as [41]

$$F_\alpha = \frac{1}{2}[g_\alpha(\mathbf{x}+\mathbf{e}_\alpha \delta t, t+\delta t) + g_\alpha(\mathbf{x},t)], \tag{2.32}$$

$$g_\alpha = w_\alpha\{A + 3\mathbf{B}\cdot[(\mathbf{e}_\alpha - \mathbf{u}) + 3(\mathbf{e}_\alpha \cdot \mathbf{u})\mathbf{e}_\alpha]\}, \tag{2.33}$$

where w_α is the weighting factor, which takes $1/3$ for $\alpha = 0$, $1/18$ for $\alpha = 1,2,\cdots,6$, and $1/36$ for $\alpha = 7,8,\cdots,18$. For Eqs. (2.1) and (2.2) here, we may just let $A = 0$ and $\mathbf{B} = \mathbf{f}$. The above scheme can handle situations with time- and space-dependent body forces or source terms, and both theoretical analysis and simulation verifications of typical examples have shown that a second-order convergence can be guaranteed within incompressible limit [41].

2.3 IBM+MRT-LBM coupling procedures

In summary, the N-S equations are solved using the LBM with external forcing term proposed by Cheng, and the fluid-structure interaction is handled by the IBM with boundary force computed by the method we described in Section 2.1.2. With the values of all variables at timestep n given, the procedures of calculating the variables at the next timestep $n+1$ are listed below:

https://doi.org/10.4208/cicp.2014.m385 Published online by Cambridge University Press

1. Knowing the boundary configuration $\mathbf{X}^n$, boundary forces $\mathbf{F}^{n+1}$ are computed using Eq. (2.17) or Eq. (2.18).
2. The boundary forces $\mathbf{F}^{n+1}$ are spread to the nearby fluid nodes via Eq. (2.7), then the Eulerian body force density $\mathbf{f}^{n+1}$ is obtained.
3. The LBM with multi-relaxation-time collision model and external force is solved to obtain the velocity field $\mathbf{u}^{n+1}$ and pressure field p^{n+1}.
4. Interpolate the velocity $\mathbf{U}^{n+1}$ of the immersed boundary from the velocity $\mathbf{u}^{n+1}$ of the nearby fluid and update the position of the immersed boundary to $\mathbf{X}^{n+1}$ by using Eq. (2.6).

3 Model verification

In order to verify the effectiveness and accuracy of the IBM+MRT-LBM coupling scheme, the relaxation processes of an inflated spherical membrane and a stretched ellipsoidal membrane immersed in three-dimensional viscous fluid are simulated, and the results are compared with the analytical solutions. The immersed boundaries considered here obey the neo-Hookean constitutive law. From now on all quantities are expressed in lattice units and time is divided by 100 for convenience. The simulations of the two cases are both carried out in a cubic domain discretized with a $64\times64\times64$ uniform lattice, if not otherwise stated. The fluid viscosity $\nu=0.1$, the initial conditions $\mathbf{u}=\{u_x,u_y,u_z\}=\{0,0,0\}$ and $p=1/3$ on the whole fluid field, the Dirichlet boundary conditions of the pressure $p=1/3$ at the six side walls which is realized by the Non-equilibrium extrapolation method, are applied for both cases.

3.1 Relaxation of an inflated spherical membrane

The initial configuration of the immersed boundary is assumed to be a spherical membrane which is inflated from its stress-free state of a smaller radius. Driven by the restoring force of the elastic boundary and the reaction of the fluid inside, the membrane will fluctuate and finally relax to an equilibrium spherical steady state, after a period of oscillation in pressure, velocity, radius, and enclosed volume. It is an appropriate benchmark case for verifying the immersed boundary method (IBM) and immersed interface method (IIM) [42] because of the strong interaction of viscous fluid and elastic boundary. When the membrane relaxes to its equilibrium steady state there is an abrupt pressure jump across the boundary which can be given analytically by [43]

$$\Delta p=\frac{2E\overline{h}}{3\overline{R}\gamma^7}(\gamma^6-1), \tag{3.1}$$

where $\overline{h}$ is the thickness of the membrane; $\gamma=R/\overline{R}$ is the radial stretching ratio, in which R and $\overline{R}$ are the radii of the membrane under deformed and stress-free states, respectively.

https://doi.org/10.4208/cicp.2014.m385 Published online by Cambridge University Press

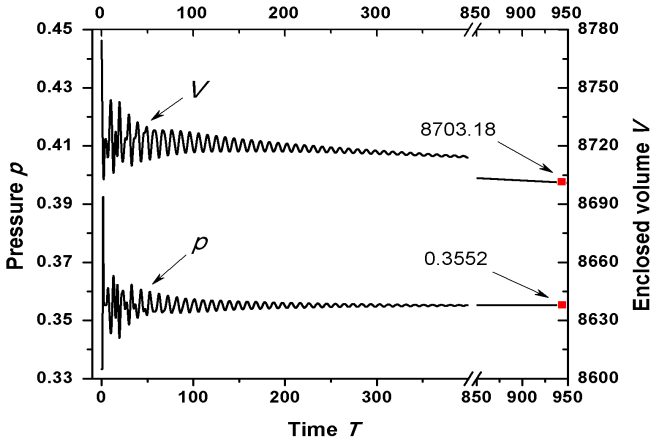


Figure 3: Histories of the center pressure and enclosed volume of the spherical membrane for $\gamma=2.0$.

In this simulation, the membrane parameters are chosen as follows: the elastic modulus $E=1.0$, the thickness $\overline{h}=0.4256$, the inflated radius $R=12.8$, and the radial stretching ratio $\gamma=1.0$ to 4.5 for different cases. Initially the membrane is inflated and placed at the center of the computational domain. The boundary is discretized by 4840 triangular elements. Fig. 3 shows the histories of the center pressure and enclosed volume of the spherical membrane for radial stretching ratio $\gamma=2.0$. The oscillating, damping and converging processes are evident. The high frequency oscillations in the volume and pressure indicate the elastic oscillating feature of the membrane boundary. The membrane eventually converges to an equilibrium state, in which the boundary elastic force is balanced by the pressure jump across the membrane. The analytical pressure difference and enclosed volume of the membrane are 0.0218 and 8784.53, while the simulated values at $T=950.0$ (95000 LBM time steps) are 0.0219 and 8703.18, which are corresponding to the very small relative errors 0.46% and 0.89%, respectively. Considering different radial stretching ratios, we obtain a series of enclosed volumes and pressure jumps, and they are plotted in Fig. 4 and listed in Table 1 for comparison with the analytical solutions. We see that the pressure accuracy and volume conservation for this case are quite good.

Table 1: Volume and pressure errors for the inflated spherical membrane of different radial stretching ratio γ at $T=950.0$.

Stretching ratio γ	1.08	1.2	1.5	2.0	2.5
Analytical V			8784.44		
Simulated V	8750.37	8734.63	8708.42	8703.18	8711.04
Error of V (%)	0.388	0.567	0.865	0.890	0.836
Analytical $\triangle p$	0.00819	0.01474	0.02006	0.02180	0.02207
Simulated $\triangle p$	0.00814	0.01491	0.02021	0.02190	0.02219
Error of $\triangle p$ (%)	0.706	1.132	0.746	0.460	0.537

https://doi.org/10.4208/cicp.2014.m385 Published online by Cambridge University Press

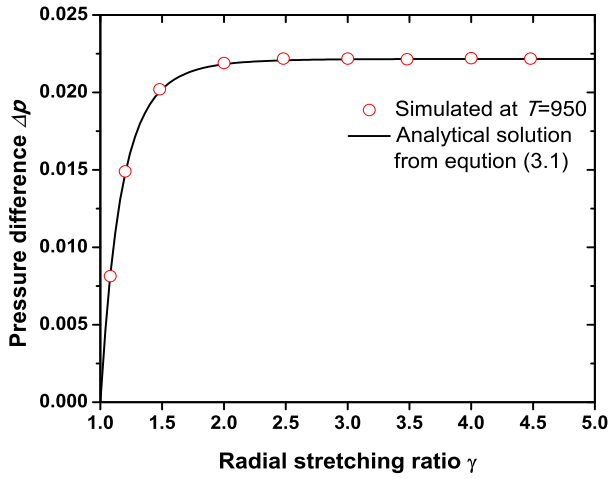


Figure 4: Pressure jumps across the spherical membrane at $T=950.0$ for different radial stretching ratios.

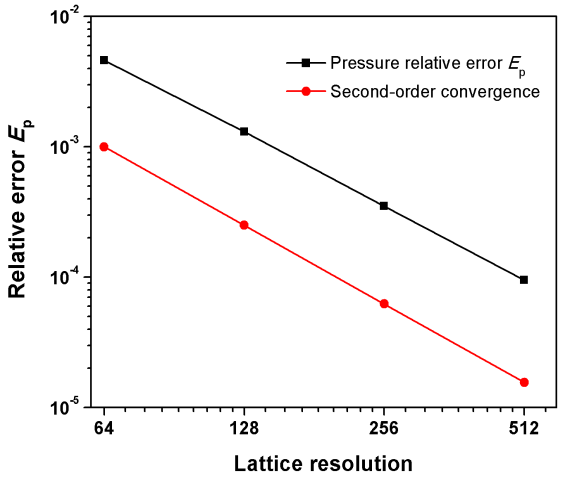


Figure 5: Spatial convergence order for the relaxation of an inflated spherical membrane.

To study the grid convergence of the present method, we keep the normalized parameters unchanged and refine the fluid lattice and boundary grid. The relative error for center pressure E_p is shown in Fig. 5 with the analytical solution given by Eq. (3.1). Generally speaking, the second-order convergence is evident, which is consistent with the accuracy of the LB method.

3.2 Relaxation of a stretched ellipsoidal membrane

Our second simulation is on the relaxation process of a stretched ellipsoidal membrane immersed in a viscous fluid. The initial boundary shape is an ellipsoid with semi-axes

https://doi.org/10.4208/cicp.2014.m385 Published online by Cambridge University Press

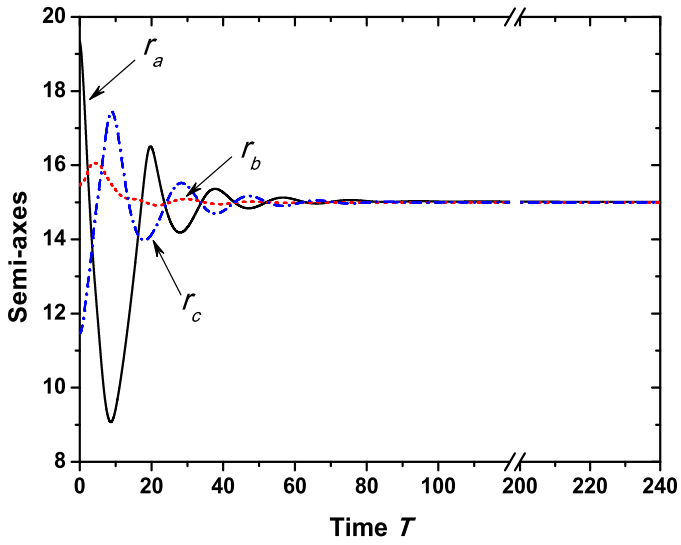


Figure 6: Oscillating histories of the ellipsoidal axes of the ellipsoidal membrane.

$(r_a,r_b,r_c)=(19.20,15.36,11.52)$, which is stretched from a sphere of radius $r\approx 15.03$. Since the fluid is assumed to be incompressible, the elastic boundary will experience a long period of oscillation and finally relax to its equilibrium spherical shape with analytical radius $r=\sqrt[3]{r_a r_b r_c}\approx 15.03$ and analytical volume $V=\frac{4}{3}\pi r_a r_b r_c=14231.79$. The immersed boundary with elastic modulus $E=0.3$ is discretized by 12990 triangular elements, and the fluid viscosity is set as 0.02. Fig. 6 shows the time evolution of the three axes of the ellipsoid, which demonstrates the shape deformation of large magnitude. The histories of the enclosed volume and center pressure are plotted in Fig. 7, which shows the high frequency of elastic force and strain oscillations. The volume is well conserved and pressure is well maintained, with relative errors at $T=240.0$ less than 0.72% and 0.03% of the analytical ones, respectively. In order to investigate the stability of the current IBM+MRT-LBM coupling scheme, Table 2 lists the maximum Re that can be achieved by reducing the viscosity, along with the enclosed volume with its corresponding relative errors. We see that the maximum Re achieved is $Re=766$, which shows very good stability characteristics compared with the traditional IBM+SRT-LBM coupling scheme.

Table 2: The enclosed volume at $T=240.0$ and the maximum Re in the relaxation process of an ellipsoidal membrane.

Given viscosity ν	0.1	0.02	0.01	0.005	0.002	0.0015
$Re_{\max}$	3.3	31.5	76.0	172.7	517.8	766.0
Analytical V			14234.42			
Simulated V	14155.78	14132.60	14103.35	14050.92	13972.28	13893.63
Error of V (%)	0.55	0.72	0.92	1.29	1.84	2.39

https://doi.org/10.4208/cicp.2014.m385 Published online by Cambridge University Press

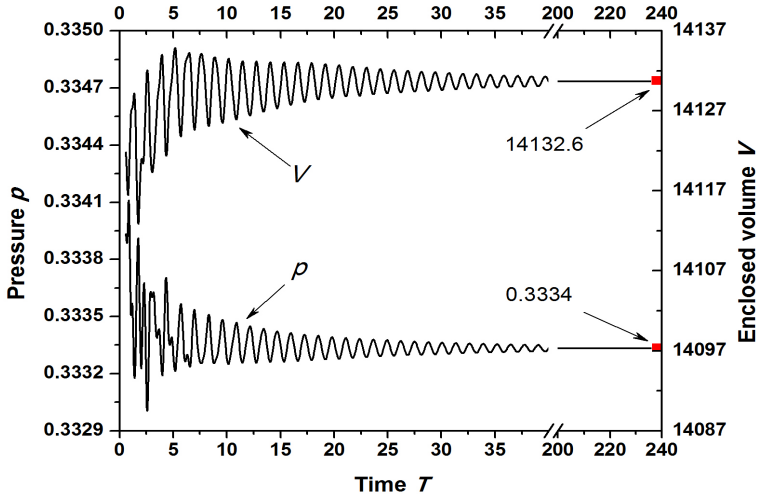


Figure 7: Oscillating histories of the center pressure and enclosed volume of the ellipsoidal membrane.

4 Simulation of 3D balloon dynamics

To further verify the IBM+MRT-LBM coupling scheme, the dynamics of a three-dimensional balloon, including the inflation, breach, and release, are simulated. Since the boundary deformation and movement are prominent and physical phenomena are abundant in these processes, the capability of handling complex FSI problems by our method can thus be demonstrated and investigated in detail.

The elastic balloon boundaries are modeled as neo-Hookean membranes. The simulations of the three cases are all carried out in a cubic domain. If not otherwise stated, the initial conditions $\mathbf{u}=\{u_x,u_y,u_z\}=\{0,0,0\}$ and $p=1/3$ on the whole fluid field, the Dirichlet boundary conditions of the pressure $p=1/3$ at the six side walls, and the fluid viscosity $\nu=0.1$, are applied.

4.1 Inflation process

The initial shape and layout of the balloon in the fluid is shown in Fig. 8, which plots the middle cross section of the three-dimensional computational domain. We use $264\times264\times264$ lattice to conduct our simulation. The immersed boundary can be divided into two parts: an elastic spherical membrane of radius $r=64.42$ and a cylindrical blowing pipe of length $0.36r$ and diameter $0.63r$, which are connected together through the tangential intersecting curve. The elastic modulus of the balloon is given as $E=1.0$, while the blowing pipe is treated as a rigid body. The rigid pipe wall is fixed by a given large fastening stiffness $k_f=10.0$ as defined by Eq. (2.18). The blowing pipe and the balloon are discretized into 5720 and 84636 triangular elements, respectively. In order to quantita-

https://doi.org/10.4208/cicp.2014.m385 Published online by Cambridge University Press

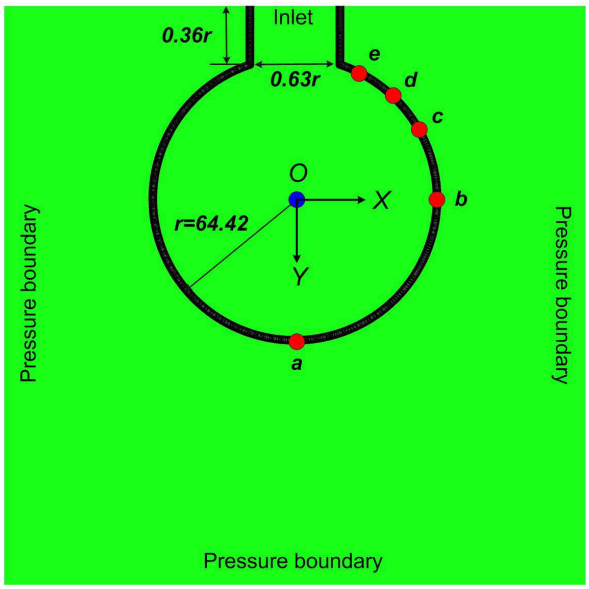


Figure 8: Initial balloon and boundary conditions for the inflation process.

tively analyze the strong interaction of the balloon and fluid flow, some probe points are assigned. As shown in Fig. 8, points **a**, **b**, **c**, **d** and **e** are particular points in the immersed boundary, and point O is at the center of the initial balloon and also set as the origin of the coordinates. When the inflation begins, a constant inflow rate of $Q = 167.97$ is imposed at the pipe inlet. We investigate the shape deformation process and place emphasis on the volume conservation and elastic wave propagating characteristics along the balloon surface.

Blown by a constant inlet flow rate, the balloon grows gradually from a sphere to a "pear" shaped bubble and then a "cherry" shaped bubble, accompanied by moderate oscillations of balloon shape and boundary surface wave. This case reflects the transformation of fluid kinetic energy to fluid pressure energy and boundary elastic energy.

The balloon configurations and streamlines at typical times are displayed in Fig. 9, which exhibits strong balloon deformation, jet flow development, and vortex formation. At the early stage of the simulation, a vortex ring is formed in the rear of the blowing pipe tips due to the injection, and the elastic surface wave is generated at the conjunction of the balloon and blowing pipe, as shown in Fig. 9(b). Then the surface wave propagates along the balloon surface and damps in particular fashion, seen in Fig. 9(c) and Fig. 9(d). The balloon inflates gradually to a larger round ball and then a "cherry" shape, while the vortex ring becomes stronger and larger, as shown in Fig. 9(e) and Fig. 9(f). The boundary surface near the balloon opening undergoes a longitudinal stretching during the "pear" shaped period and undergoes a transversal stretching during the "cherry" shaped period, because the opening is constrained by the blowing pipe.

https://doi.org/10.4208/cicp.2014.m385 Published online by Cambridge University Press

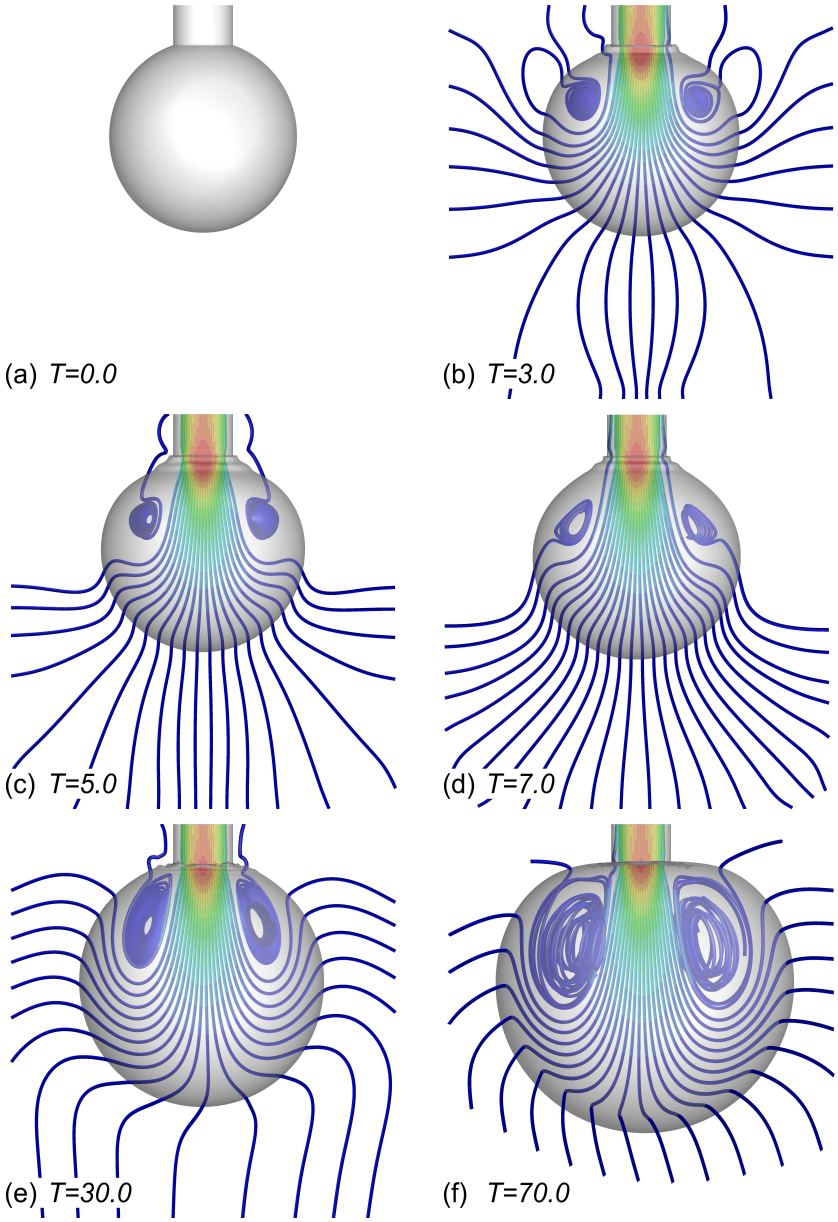


Figure 9: Streamlines and balloon configurations at different times of the inflation process.

Fig. 10 shows the velocity vectors and pressure distribution at typical times $T=10.0$, 15.0, 20.0, 30.0, 50.0 and 70.0. When the fluid is injected into the balloon, the inside pressure increases gradually with an abrupt pressure jump across the balloon surface. On the other hand, Fig. 11 shows the coordinates of Y_a and X_b of probe points **a** and **b** on the balloon surface. Y_a and X_b grow in a wavy manner at the early stage of the injection,

https://doi.org/10.4208/cicp.2014.m385 Published online by Cambridge University Press

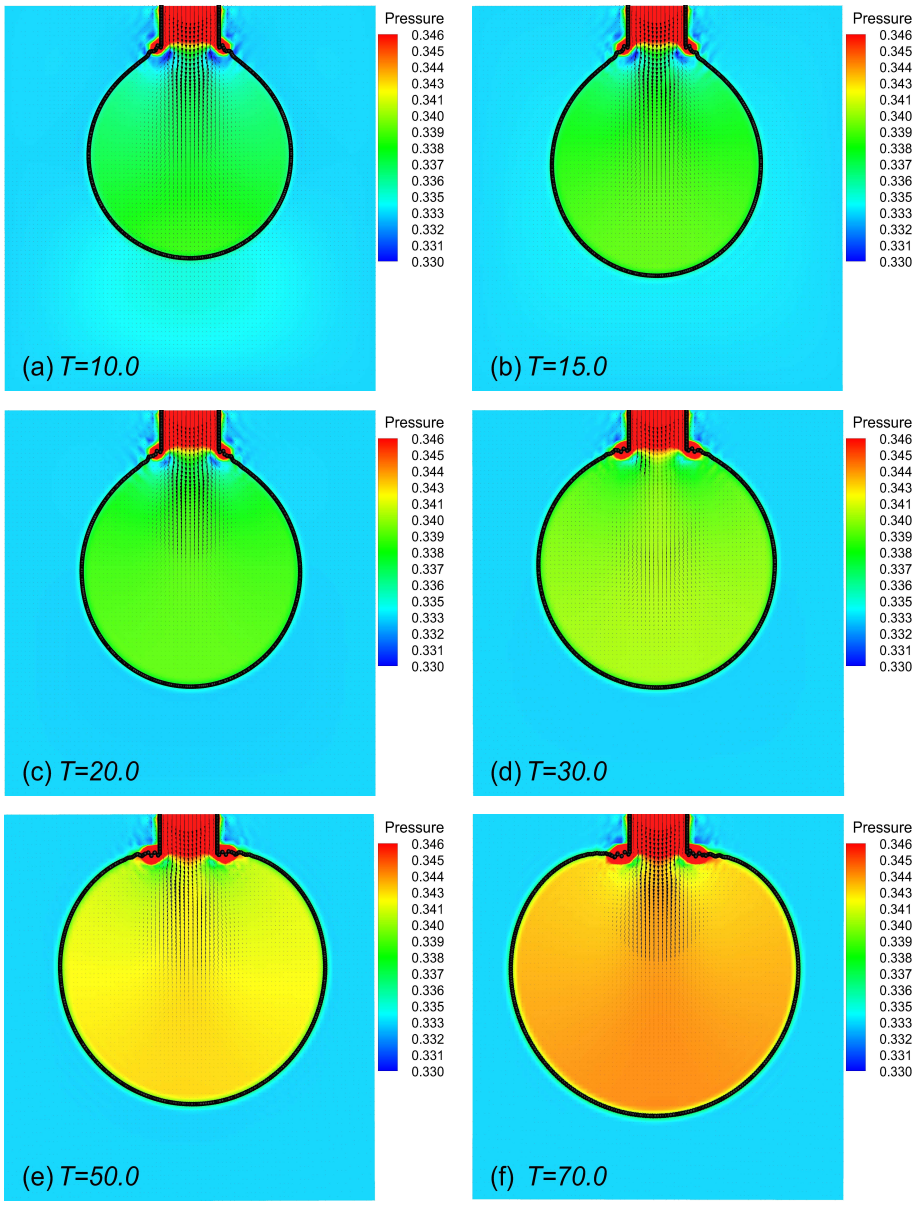


Figure 10: Velocity vectors and pressure distribution at different times of the inflation process.

indicating the different longitudinal and transversal expansions. The larger gradient of X_b before $T=5.0$ shows the faster transversal expansion, and the steeper grow of Y_a from $T=5.0$ to 15.0 represents the faster longitudinal expansion.

Fig. 12 shows the histories of the radii of points **c**, **d** and **e** from the origin O. The propagation characteristics of elastic surface wave are roughly captured by the wavy fluctuations and phase differences of the radius curves in the early time.

https://doi.org/10.4208/cicp.2014.m385 Published online by Cambridge University Press

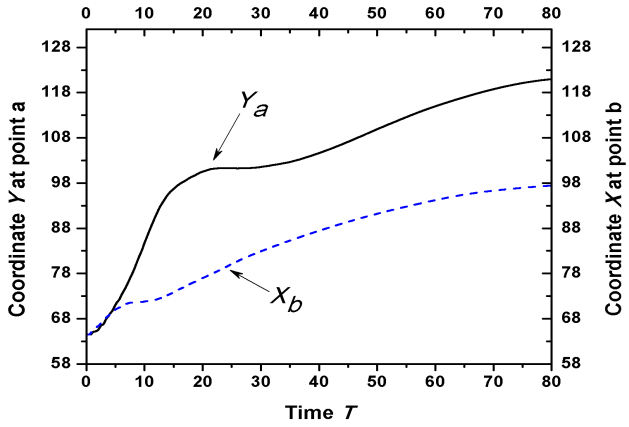


Figure 11: Histories of Y_a and X_b of probe points **a** and **b** in the inflation process.

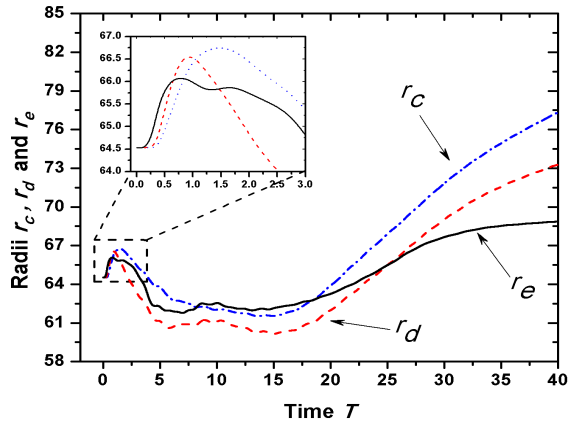


Figure 12: Histories of the radii of probe points **c**, **d** and **e** at the balloon surface in the inflation process.

Due to the incompressibility of fluid, the increase rate of balloon volume should be equal to the inflow rate. The histories of the enclosed volume and center pressure are shown in Fig. 13. It is obvious that the enclosed volume increases linearly with a gradient $k_v = 166.57$, which is corresponding to a relative volume error 0.83% compared with the inlet flow rate $Q = 167.97$, indicating a very good volume conservation property. The pressure increases and fluctuates with high frequency, indicating the boundary elastic wave is superposed to the low frequency shape-deforming wave shown in the previous figures.

4.2 Breach process

When the balloon is inflated to a certain degree, the pressure across the balloon surface becomes so high that the balloon is no longer able to resist the stress needed to balance

https://doi.org/10.4208/cicp.2014.m385 Published online by Cambridge University Press

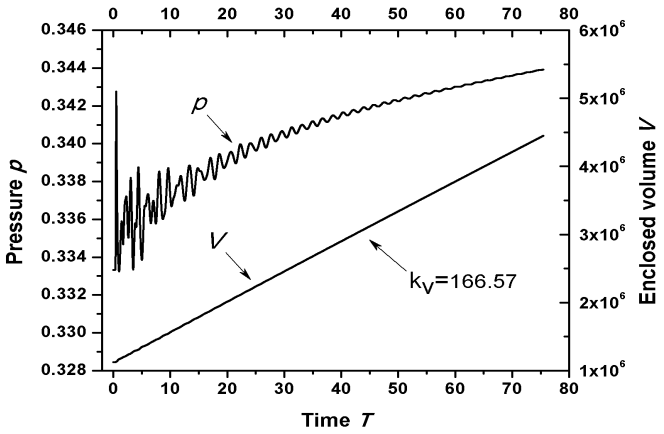


Figure 13: Oscillating histories of the center pressure and enclosed volume in the inflation process.

the pressure jump, and a breach will occur somewhere. Driven by the pressure difference between the inside and outside of the balloon, the fluid will squirt outward through the breached opening and result in a decrease of the pressure difference across the balloon surface. In this process, the elastic strain energy stored during the inflation process will be transformed into the fluid kinetic energy, which will attenuate gradually owing to fluid viscosity. We try to simulate this strong interaction using the IBM+MRT-LBM coupling scheme.

The layout of the initially inflated balloon is shown in Fig. 14, with all the parameters kept unchanged compared to the inflation process, except that the inlet is switched to

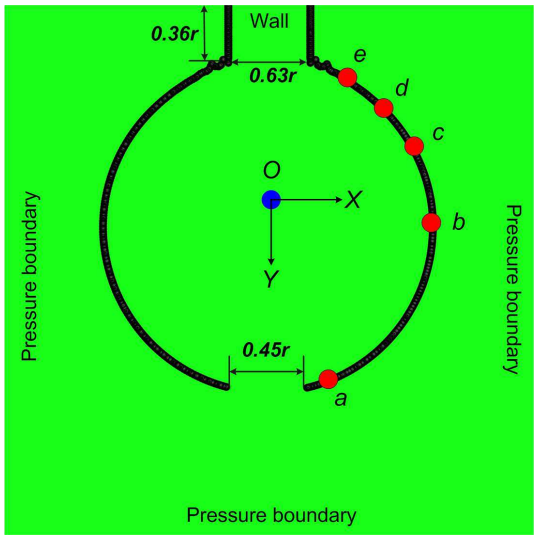


Figure 14: Initial balloon shape and boundary conditions for the breach process.

https://doi.org/10.4208/cicp.2014.m385 Published online by Cambridge University Press

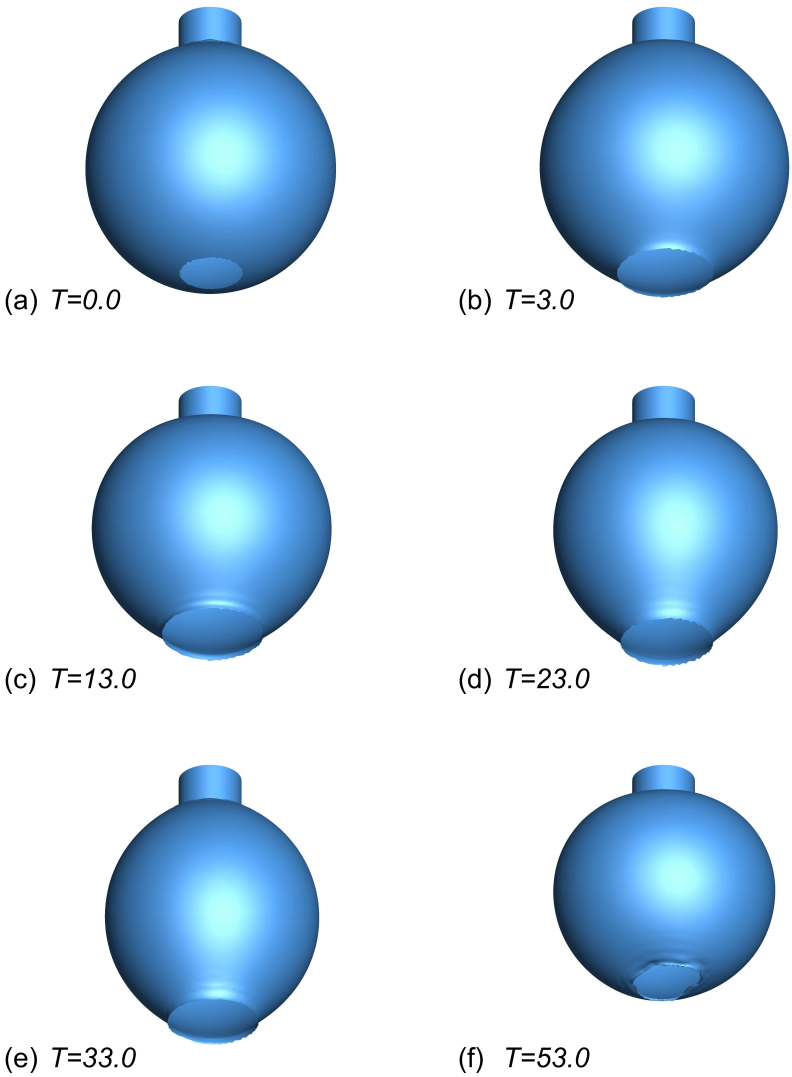


Figure 15: Balloon configurations at different times in the breach process.

wall and a breach of radius $0.45r$ is imposed at the balloon apex. These initial conditions are achieved by the above inflation process, in which the balloon is inflated to a certain degree and there exist a pressure jump across the balloon surface. The probe points are also selected like the inflation process except that point **a** is moved to the breach rim.

This breach process can clearly demonstrate the phenomena of sudden stress release at free edges, shape deformation due to energy transformation and dissipation, and elastic surface wave propagation.

Fig. 15 shows the balloon configurations at some typical times. Significant widening

https://doi.org/10.4208/cicp.2014.m385 Published online by Cambridge University Press

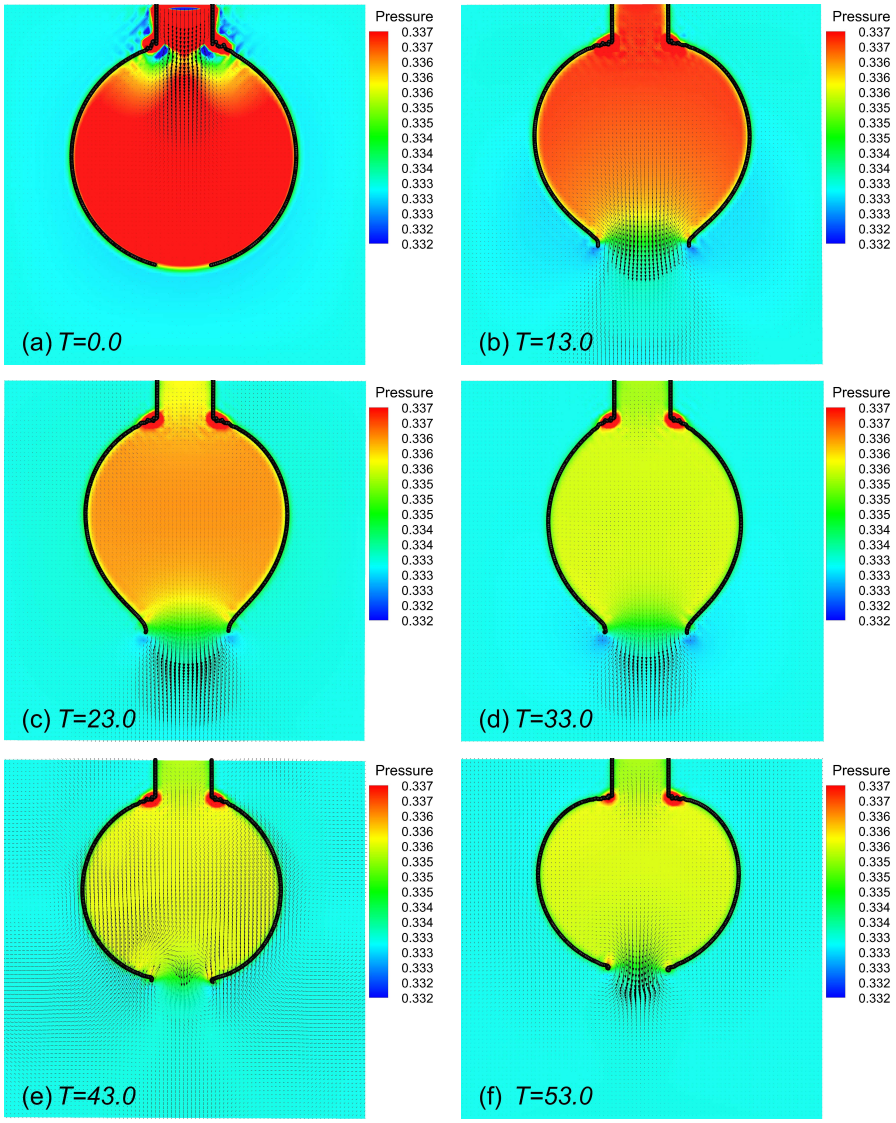


Figure 16: Velocity vectors and pressure distribution at different times in the breach process.

of the breached opening can be observed at the early stage as shown in Fig. 15(b), indicating a stress release phenomenon. Due to the strong fluid structure interaction, several corrugations are generated at the vicinity of the breach rim (Fig. 15(c)). As the breach process continues, the balloon elongates forming a "lemon" shape (Fig. 15(d) and Fig. 15(e)). Finally, when the pressure difference across the balloon surface gradually attenuates to zero, the balloon recovers its reference spherical configuration by strong contraction from its former "lemon" shape, and the corrugations reappear (Fig. 15(f)).

Fig. 16 shows the velocity vectors and pressure distributions at different times. The

https://doi.org/10.4208/cicp.2014.m385 Published online by Cambridge University Press

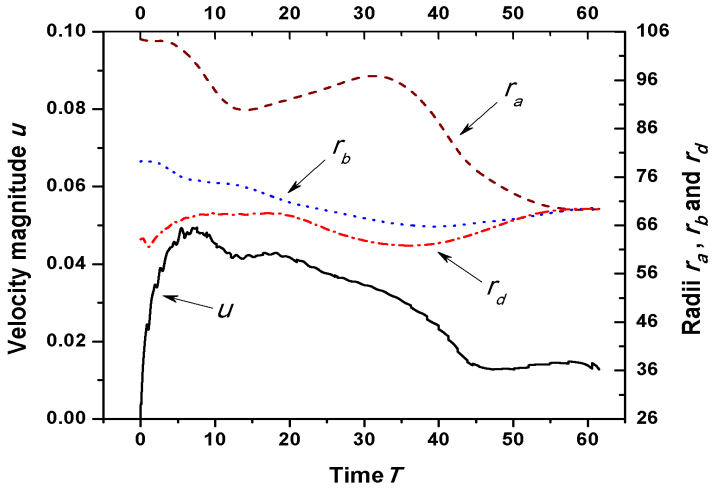


Figure 17: Histories of velocity magnitude at the breach and r_a, r_b and r_d of probe points **a**, **b** and **d** in the breach process.

pressure jump across the balloon surface is gradually decreasing as the fluid is flowing out and the boundary is relaxing. The expanding and contracting of the breached opening and the shape deformation accompanied by pressure and elastic energy release are also clear.

In order to investigate the breach process in detail, we plot the velocity magnitude at the breach and the radii of points **a**, **b** and **d** from origin O in Fig. 17. In the early stage, the curves of points **a** and **b** drop down while the curve of point **d** goes up, which indicate strong contraction and recoil effects. After approximate $T=2.0$, the balloon start to elongate, leading to a slight increase of curve r_a. The r_a reaches its peak around $T=33.0$, corresponding to the obviously "lemon" shaped stage. After that the pressure difference across the boundary and the balloon strain energy attenuate sufficiently, the balloon gradually recover its stress-free state, and the r_a curve eventually drops down with reduced slope and finally coincides with the curves r_a and r_d. Due to the large pressure difference across the balloon surface formed by the inflation, the history curve of jet velocity magnitude u grows very fast at the early stage with high frequency oscillation superposed. The curve u attains its maximum value at approximately $T=6.0$ and then slightly drops down before reaching a relatively flat phase. With the further decrease of pressure jump, the u curve drops down again and eventually become horizontal as the balloon approaches its equilibrium state.

The pressure in the origin point O and the total strain energy of the balloon are plotted in Fig. 18. The pressure curve goes down gradually with the high frequency boundary elastic wave superposed. The energy and pressure curves become flat after $T=50.0$, and eventually approach a horizontal line indicating that the balloon reaches its equilibrium state.

https://doi.org/10.4208/cicp.2014.m385 Published online by Cambridge University Press

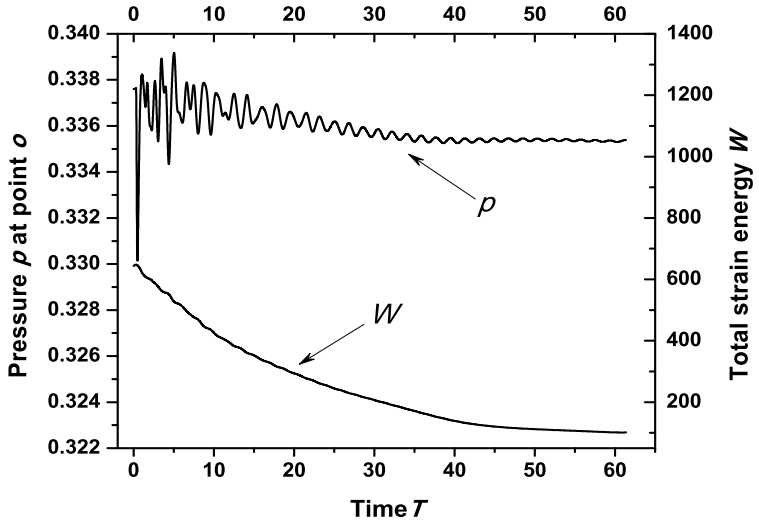


Figure 18: Histories of the total strain energy and pressure at origin O in the breach process.

4.3 Release process

Releasing an inflated balloon will cause the fluid spurting outward and the balloon moving in the opposite direction according to the momentum conservation law. This recoil phenomenon may be successfully captured by the IBM+MRT-LBM scheme without any modification. To verify the capability of present scheme, the release process of an inflated spherical balloon is simulated.

Fig. 19 shows the initial and boundary conditions. The balloon is initially placed in the center of a cubic computational domain and the center of the balloon is set as the origin of the coordinates. Initially, an abrupt pressure jump across the balloon surface is imposed to balance the restoring boundary force. The velocity is set to zero in the whole domain. The above state can be achieved by the relaxation process of a spherical membrane we have described in Section 3.1 with the radial stretching ratio $\gamma = R/\overline{R} = 2$ and elastic modulus $E = 1.5$. The computational domain and the balloon boundary are discretized into a $200 \times 200 \times 200$ lattice and 52321 triangular elements, respectively. Just like the breach case, we artificially remove a certain piece of boundary surface to form a breached opening, which generates the starting point of our simulation.

Fig. 20 shows the balloon configurations at different times. After the breach is formed, the sudden stress release leads to significant widening of the breach opening and the balloon is not quick to recoil in the opposite direction but to contract in the original position for a while, as shown in Fig. 20(b). This represents the fluid acceleration stage. After $T = 3.0$, the boundary elastic force accelerates the surrounding fluid and the balloon start to recoil in the opposite direction as shown in Fig. 20(c), in which the balloon is squished into an ellipsoidal shape from its original spherical shape due to the retardation of the fluid. The balloon overcomes the fluid drag and recoils in an accelerating manner until it

https://doi.org/10.4208/cicp.2014.m385 Published online by Cambridge University Press

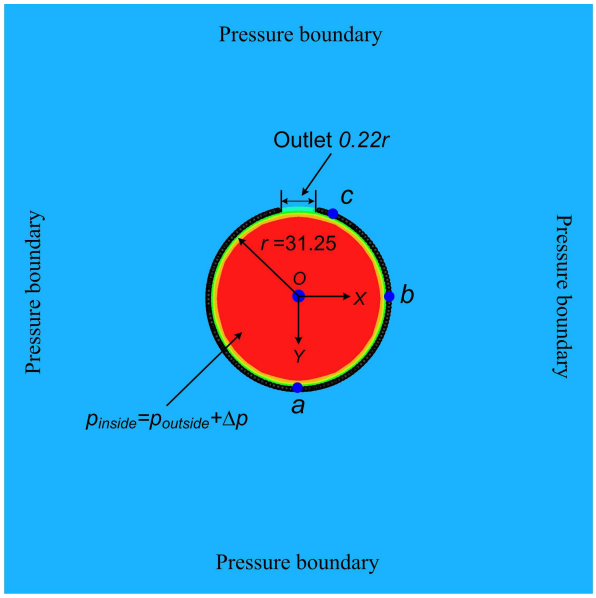


Figure 19: Initial balloon and boundary conditions for the release process.

reaches the edge of the computational domain, as shown in Fig. 20(d)-(f). It is worth noting that several corrugations can be observed at the breach rim during the recoil process, which is the indication of the elastic wave propagating along the balloon surface.

Fig. 21 shows the pressure distributions and velocity vectors at different times. At the beginning of the simulation there is an abrupt pressure jump across the balloon surface and the velocity is zero (Fig. 21(a)). Driven by the pressure difference across the boundary, the fluid starts to spurt outward through the breach and form a vortex ring just beside the breach (Fig. 21(b)). As the vortex develops to a certain degree, the upper part of the balloon starts to move in the Y-direction while the lower part of the balloon still sticks to its original position, which makes the balloon look like a pedicel removed "tomato" (Fig. 21(c)). At $T = 5.0$, the recoil effect becomes dominant and the balloon recovers its spherical shape while moving in the opposite direction with an accelerated speed, as shown in Fig. 21(e) and Fig. 21(f).

The contraction and recoil process can be addressed more clearly by Fig. 22, in which the histories of Y coordinates of points **a**, **b** and **c** are plotted. In the early time, all three curves remain flat until a certain time around $T = 1.0$ to 3.0 when the curves start to drop down, indicating that the balloon stays and contracts at its original position for a while before recoil effect becomes dominant, which is consistent with the observation in Fig. 21. It is worth noting that the starting points for descending of the three curves are different, with point **c** experiencing almost no delay and point **a** experiencing the longest delay. This non-synchronization phenomenon indicates that the balloon is squished into the ellipsoidal shape from its original spherical shape. In Fig. 23, the histories of X coordinates

https://doi.org/10.4208/cicp.2014.m385 Published online by Cambridge University Press

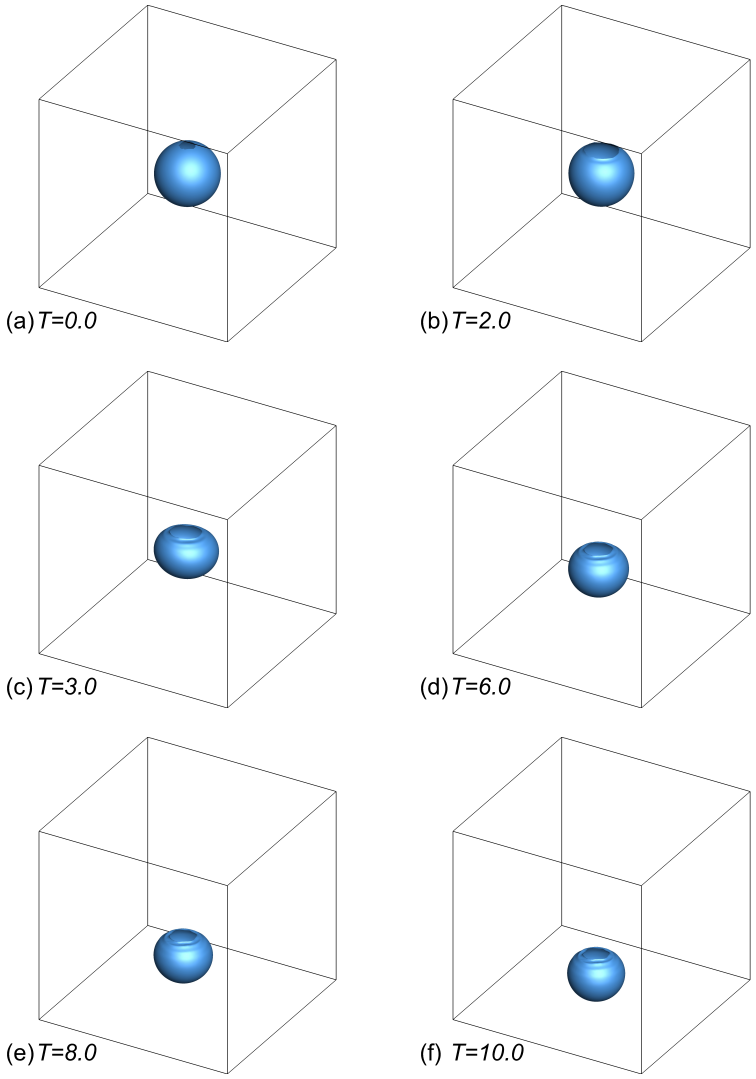


Figure 20: Balloon configurations at different times in the release process.

of points **a**, **b** and **c** along with the velocity magnitude u at the breach are plotted. The developing trend of curves X_b and X_c can be interpreted similarly to Fig. 22. The history curve of jet velocity u increases rapidly at the very early stage due to the large pressure difference and then slows down owing to the significant widening of the breach opening. The curve reaches its maximum value at approximately $T=2.5$, corresponding to the top of the hump shape of curve X_c. After $T=2.5$, the curve exhibits strong oscillations, indicating the strong interaction between fluid and the elastic balloon and frequent transformation between strain energy and fluid kinetic energy.

https://doi.org/10.4208/cicp.2014.m385 Published online by Cambridge University Press

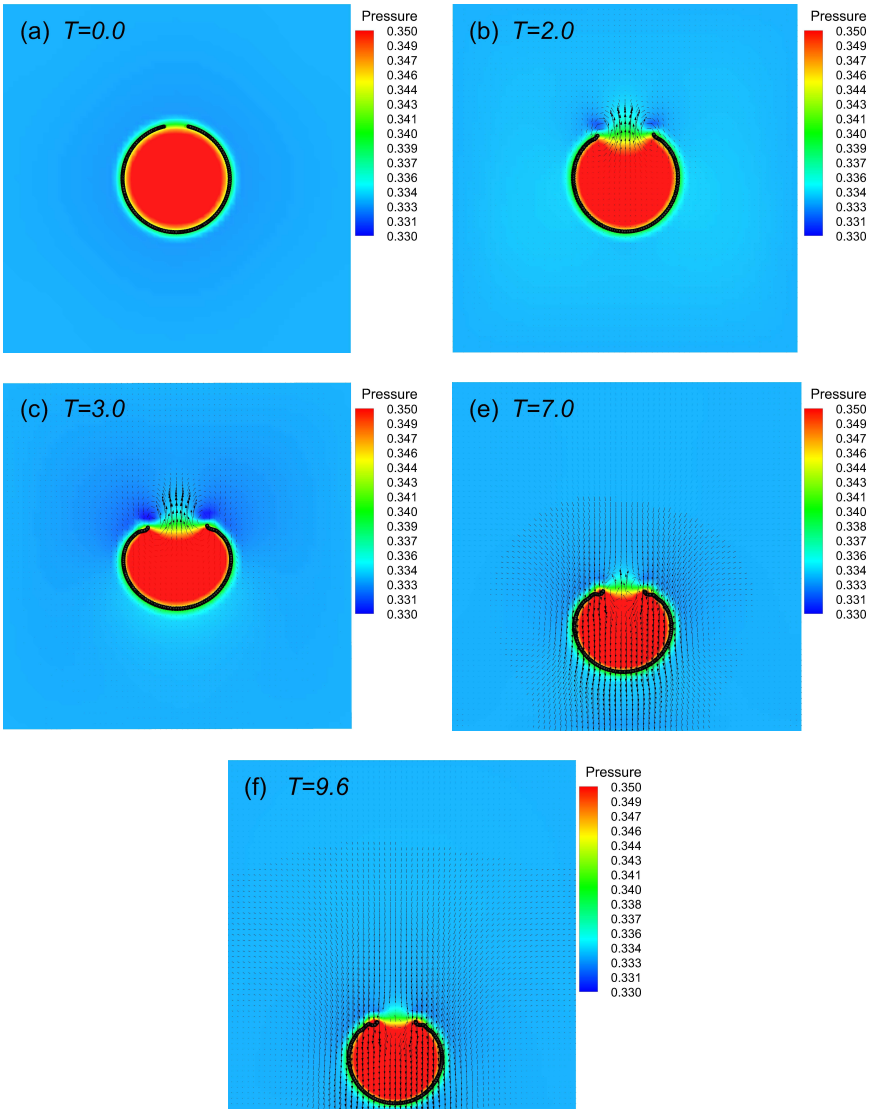


Figure 21: Velocity vectors and pressure distribution at different times in the release process.

5 Conclusions

The IBM+MRT-LBM coupling scheme, suitable for three-dimensional flexible boundary FSI problems with rapid boundary motion and large pressure gradient, is proposed. The very good characteristics in pressure retention, volume conservation, and numerical stability are first verified by two typical benchmark cases. To further verify the capability of the IBM+MRT-LBM scheme, the three-dimensional balloon dynamics including infla-

https://doi.org/10.4208/cicp.2014.m385 Published online by Cambridge University Press

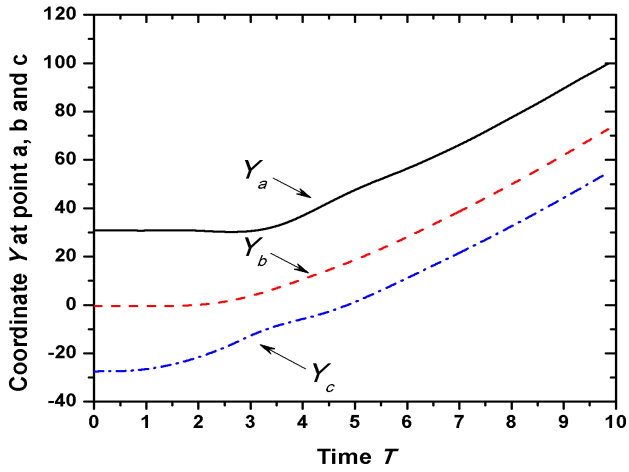


Figure 22: Histories of Y_a, Y_b and Y_c of probe points **a**, **b** and **c** in the release process.

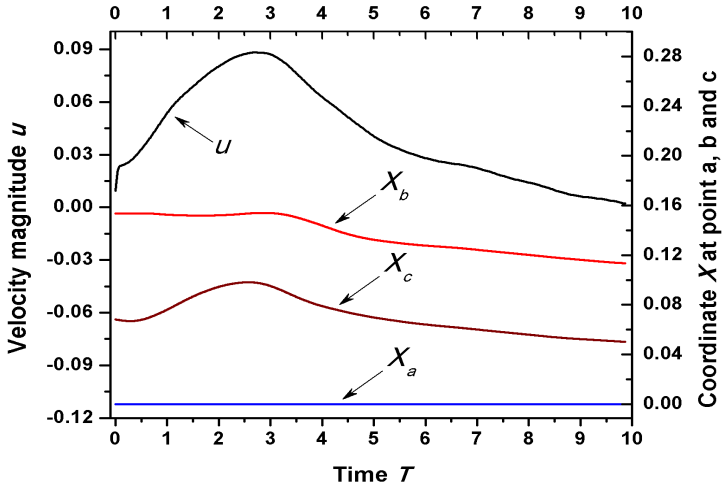


Figure 23: Histories of velocity magnitude at the breach and X_a, X_b and X_c of probe points **a**, **b** and **c** in the release process.

tion process, breach process, and release process, are simulated. The profound physical phenomena, such as propagation of elastic boundary wave, oscillation of boundary configuration, recoil effect of fluid to structure, and the stress release in the free edge, are all observed. These demonstrate that our scheme can properly handle complicated three-dimensional FSI problems involving large deformation and large pressure gradient. We shall apply the scheme in the future to more realistic problems, such as the formation and rupture of atherosclerosis plaques in carotid bifurcations.

https://doi.org/10.4208/cicp.2014.m385 Published online by Cambridge University Press

Acknowledgments

This work was supported by the National Natural Science Foundation of China (NSFC, Grant numbers 10572106, 10872153 and 11172219) and the Specialized Research Fund for the Doctoral Program of Higher Education of China (Grant No.20130141110013).

References

[1] C. S. Peskin, Flow Patterns Around Heart Valves: A Digital Computer Method for Solving the Equations of Motion, PhD thesis, Physiol, Albert Einstein Coll. Med., Univ. Microfilms, 378 (1972), 72-102.
[2] D. M. McQueen, and C. S. Peskin, A three-dimensional computer model of the human heart for studying cardiac fluid dynamics, Comput. Graphics, 34 (2000), 56-60.
[3] I. Borazjani, Fluid-structure interaction, immersed boundary-finite element method simulations of bio-prosthetic heart valves, Comput. Method. Appl. M., 257(2003), 103-116.
[4] R. Dillon, L. Fauci and D. Gaver III, A microscale model of bacterial swimming, chemotaxis and substrate transport, J. Theor. Biol., 177(1995), 325-340.
[5] L. J. Fauci, and C. S. Peskin, A computational model of aquatic animal locomotion, J. Comput. Phys., 77 (1988), 85-108.
[6] J. F. Zhang, P. C. Johnson, and A. S. Popel, An immersed boundary lattice Boltzmann approach to simulate deformable liquid capsules and its application to microscopic blood flows, Phys. Biol., 4 (2007), 285-295.
[7] J. F. Zhang, P. C. Johnson, and A. S. Popel, Red blood cell aggregation and dissociation in shear flows simulated by lattice Boltzmann method, J. Biomech., 41 (2008), 47-55.
[8] Y. Sui, Y. T. Chew, P. Roy and H. T. Low, A hybrid method to study flow-induced deformation of three-dimensional capsules, J. Comput. Phys., 227(2008), 6351-6371.
[9] T. Krüger, F. Varnik, and D. Raabe, Efficient and accurate simulations of deformable particles immersed in a fluid using a combined immersed boundary lattice Boltzmann finite element method, Comput. Math. Appl. M., 61(2011), 3485-3505.
[10] L. D. Zhu, and C. S. Peskin, Simulation of a flapping flexible filament in a flowing soap film by the immersed boundary method, J. Comput. Phys., 179(2002), 452-468.
[11] L. D. Zhu, G. W. He and S. Z Wang, et al. An immersed boundary method based on the lattice Boltzmann approach in three dimensions, with application, Comput. Math. Appl. M., 61(2011), 3506-3518.
[12] J. Hao and L. D. Zhu, A 3D implicit immersed boundary method with application,Theor. Appl. Mech. Lett., 6(2011), 062002.
[13] Y. Kim, and C. S. Peskin, 2-D Parachute simulation by the immersed boundary method, SIAMJ. Sci. Comput., 28 (2006), 2294-2312.
[14] Y. Kim, and C. S. Peskin, 3-D Parachute simulation by the immersed boundary method, Comput. Fluids., 38 (2009), 1080-1090.
[15] Y. H. Qian, D. d'Humières and P. Lallemand, Lattice BGK models for Navier-Stokes equation, Europhys. Lett., 17(1992),479-484.
[16] H. D. Chen, S. Y. Chen and W. H. Matthaeus, et al. Recovery of the Navier-Stokes equations using a lattice-gas Boltzmann method, Phys. Rev. A, 45(1992), R5339-R5342.
[17] S. Chen, and G. D. Doolen, Lattice Boltzmann method for fluid flows, Annu. Rev. Fluid. Mech., 30 (1998), 329-364.

https://doi.org/10.4208/cicp.2014.m385 Published online by Cambridge University Press

[18] H. W. Zheng, C. Shu, and Y. T. Chew, A lattice Boltzmann model for multiphase flows with large density ratio, J. Comput. Phys., 218 (2006), 353-371.
[19] J. Tölke and M. Krafczyk, TeraFLOP computing on a desktop PC with GPUs for 3D CFD, Int. J. Comput. Fluid. D., 22(2008), 443-456.
[20] Z. G. Feng, and E. E. Michaelides, The immersed boundary-lattice Boltzmann method for solving fluid-particles interaction problems, J. Comput. Phys., 195 (2004), 602-628.
[21] Y. G. Cheng and H. Zhang, Immersed boundary method and lattice Boltzmann method coupled FSI simulation of mitral leaflet flow, Comput. Fluids, 39(2010), 871-881.
[22] F. B. Tian, H. X. Luo, L. D. Zhu, and J. C. Liao, et al, An efficient immersed boundary-lattice Boltzmann method for the hydrodynamic interaction of elastic filaments, J. Comput. Phys., 230(2011), 7266-7283
[23] A. Dupuis, P. Chatelain, and P. Koumoutsakos, An immersed boundary-lattice Boltzmann method for the simulation of the flow past an impulsively started cylinder, J Comput. Phys., 227 (2008), 4486-4498.
[24] X. D. Niu, C. Shu, Y. T. Chew, and Y. Peng, A momentum exchange-based immersed boundary-lattice Boltzmann method for simulating incompressible viscous flows, Phys. Lett. A., 354 (2006), 173-182.
[25] Y. Peng and L. S. Luo, A comparative study of immersed-boundary and interpolated bounce-back methods in LBE, Prog. Comput. Fluid. Dy.,(2008), 156-167.
[26] S. K. Kang and Y. A. Hassan, A comparative study of direct-forcing immersed boundary-lattice Boltzmann methods for stationary complex boundaries, Int. J. Numer. Meth. Fluids, 66(2011)1132-1158.
[27] Y. G. Cheng, H. Zhang and C. Liu, Immersed Boundary-Lattice Boltzmann Coupling Scheme for Fluid-Structure Interaction with Flexible Boundary, Commun. Comput. Phys., 9(2011),1375-1396.
[28] J. Wu and C. Shu, Implicit velocity correction-based immersed boundary-lattice Boltzmann method and its applications, J. Comput. Phys., 228(2009), 1963-1979.
[29] Z. L. Guo, C. G. Zheng and B. C. Shi, Discrete lattice effects on the forcing term in the lattice, Physical Review E, 65(2002), 46308.
[30] J. Hao, and L. D. Zhu, A lattice Boltzmann based implicit immersed boundary method for fluid–structure interaction, Comput. Math. Appl., 59(2010), 185-193.
[31] d'Humières, I. Ginzburg, M. Krafczyk, P. Lallemand, and L. S. Luo, Multiple-relaxation time lattice Boltzmann models in three dimensions, Philos. Trans. Royal. Soc. A, 360 (2002), 437-451.
[32] P. Lallemand, and L. S. Luo, Theory of the lattice Boltzmann method: dispersion, dissipation, isotropy, Galilean invariance, and stability, Phys. Rev. E, 61(6) (2000), 6546-6562.
[33] Y. Peng, and C. Shu et al., Application of multi-block approach in the immersed boundary lattice Boltzmann method for viscous fluid flows, J. Comput. Phys., 218 (2006), 460-478.
[34] Y. Peng, L. S. Luo and J. Gounley, Study of biopartical transport using Lattice Boltzmann method and immersed boundary method, in 10th ICMMES. 2013.
[35] C. S. Peskin, The immersed boundary method, Acta numerica., 11(2002),479-517.
[36] J. M. Charrier,S. Shrivastava and R. Wu, Free and constrained inflation of elastic membranes in relation to thermoformingłnon-axisymmetric problems, J. Strain. Anal. Eng., 24(1989), 55-74.
[37] S. Shrivastava and J. Tang, Large deformation finite element analysis of non-linear viscoelastic membranes with reference to thermoforming, J. Strain. Anal. Eng., 28(1993), 31-51.

https://doi.org/10.4208/cicp.2014.m385 Published online by Cambridge University Press

[38] C. D. Eggleton and A. S. Popel, Large deformation of red blood cell ghosts in a simple shear flow, Phys. Fluids, 10(1998), 1834-1845.
[39] S. K. Doddi and P Bagchi, Lateral migration of a capsule in a plane Poiseuille flow in a channel, Int. J. Multiphas. Flow, 34(2008), 966-986.
[40] D. Barthes-Biesel, A. Diaz and E. Dhenin, Effect of constitutive laws for two-dimensional membranes on flow-induced capsule deformation, J. Fluid. Mech., 460(2002), 211-222.
[41] Y. G. Cheng, and J. P. Li, Introducing unsteady non-uniform source terms into the lattice Boltzmann model, Int. J. Numer. Meth. Fluids, 56 (2008), 629-641.
[42] L. Lee, and R. J. LeVeque, An immersed interface method for incompressible Navier-Stokes equations, SIAM J. Sci. Comput., 25 (2003), 832-856.
[43] F. Gruttmann and R. L. Taylor, Theory and finite element formulation of rubberlike membrane shells using principal stretches, Int. J. Numer. Meth. Engng., 35(1992), 1111-1126.

https://doi.org/10.4208/cicp.2014.m385 Published online by Cambridge University Press